Volume 1 | Number 1 | Jan 2013 | Pages 1–100

PCCP

Physical Chemistry Chemical Physics
www.rsc.org/pccp

ROYAL SOCIETY OF CHEMISTRY

ROYAL SOCIETY OF CHEMISTRY

www.rsc.org/pccp

Why Bromine Squares Palladium Off? An *Ab Initio* Study of Brominated Palladium and its Nanomorphology

Su-Hyun Yoo,[1] Ji-Hwan Lee,[1] Bernard Delley,[2] and Aloysius Soon[1, *]

[1]*Global E3 Institute and Department of Materials Science and Engineering,*
Yonsei University, Seoul 120-749, Korea

[2]*Condensed Matter Theory Group, Paul Scherrer Institut, CH-5232 Villigen, Switzerland*

(Dated: July 10, 2014)

Abstract

A first-principles description and prediction of brominated nanoscrystals of Pd is presented. In particular, we conducted an extensive study of the adsorption behaviour of Br on various Pd surfaces (including both low and high Miller-index surfaces) as a function of its surface coverage. Coupling our calculated surface energies with *ab initio* (electrochemical) thermodynamics and the Gibbs-Wulff shape model, we find that the relative stability of the Pd surfaces are strongly modified by Br, allowing high Miller-index surfaces of Pd (namely the (210) surface) to become competitively favourable at moderate concentrations of Br. We also show that Pd nanoparticles assume a cube-like crystal shape at high concentrations of Br, exposing mainly the (100) facets with a Br surface coverage of 0.5 ML. This not only confirms and explains recent solution synthesis results, but also provides a quantitative atomic picture of the exposed surface facets, which is crucial in understanding the local surface chemistry of shape-controlled nanoparticles for better nanocatalyst design.

Graphical Abstract for Table-of-Content:

We study the chemisorption of Br on the low and high Miller-index surfaces of Pd nanoparticles, and provide a quantitative atomic picture of the surface chemistry and physics of these brominated nanoparticles for a rational and systematic design of more selective and active Pd shape-sculptured nanocatalysts.
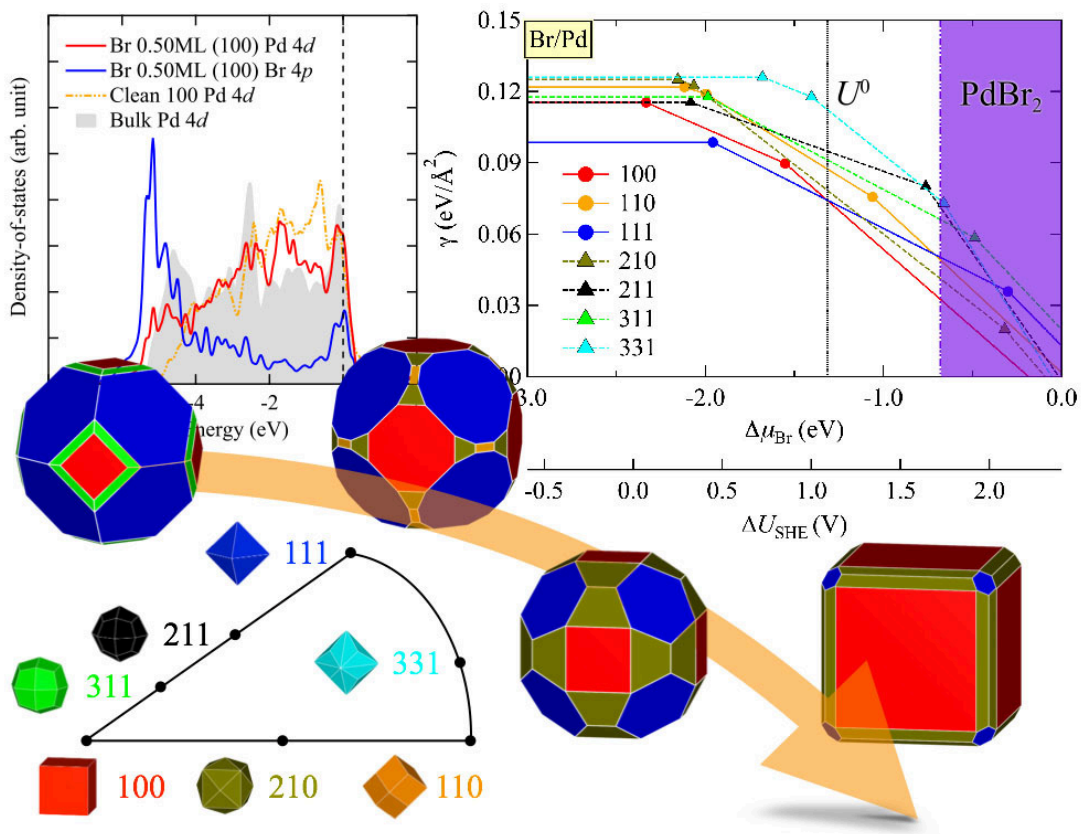
I. INTRODUCTION

Transition metals and their alloys have been actively investigated for several decades due to their promising properties, such as surface plasmon, magnetism and applications toward electrodes and catalysts.[1,2] Because transition metals have multiple oxidation state, they exhibit good catalytic performance towards various chemical reactions, for example, oxygen reduction reaction (ORR).[3,4] With the advancement of nanoscience and nanotechnology in recent years, nanostructures of transition metals very often give rise to a large enhancement in catalytic performance, due to the fact that the ratio of surface-to-volume of these nano-materials is greatly increased. Given that the overall selectivity of the nanocatalyst can be tuned via controlling its exposed surfaces,[5,6] many have now focused not only on gaining an understanding of how to control the size of the nanoparticles, but also on studying its explicit crystal shape or nanomorphology to display various unique chemical and physical properties at the nanoscale.[7–9]

Very commonly, halides (F, Cl, Br, and I) have been widely used in controlling and manipulating the shape of transition metal nanoparticles. This is due to the fact that halide ions tend to interact strongly on the exposed metal facets, explicitly exhibiting a strong influence on its surface energetics and growth kinetics. For instance, it was shown that Cu nanoparticles could assume a nanocube shape under a Cl environment,[10] while another work demonstrated that different halides (Cl and I) could potentially show drastically different polarization effects on Cu surfaces.[11] In addition, the assistance of Au nanorod and nanoplate synthesis by the introduction of Br and I, respectively, have been reported and studied.[12]

Palladium, being one of the (platinum group) late transition metals, has been used in a variety of important technological applications, such as electrodes for multilayer ceramic capacitor,[13,14] hydrogen storage,[15,16] hydrogenation reaction[17] and the Suzuki coupling reaction.[18,19] For pristine nanoparticles of Pd, it has a naturally truncated octahedron shape due to its most stable (111) facets. Recently, it was found that Pd(100) shows a good catalytic performance for a methane oxidation reaction when compared to that of other Pd surfaces, such as the (111), (211) and (321) surfaces.[20] This signals that a cube-shaped Pd nanoparticle could be a robust catalyst for this type of chemical reactions. Indeed, some recent experiments on the synthesis of cube-shaped Pd nanoparticles have been reported.[12,21,22] In case of (100)-encapsulated nanocubes of Pd, a KBr solution environment with the pre-

cursor Na_2PdCl_4 was found to be essential for achieving these Pd nanocubes.[21–23] The use of the KBr solution as inorganic capping agents/ligands in these experiments offers a distinct advantage over the commonly used organic surfactant bromides (e.g. hexadecyltrimethylammonium bromide, CTAB), where the long-chain organic groups that could sterically block the local catalytic sites.[24] In addition, cube-shaped Pt-Pd bimetallic nanoparticles have also been realized via the use of Br ions.[25]

Although there have been much success in the experimental approaches to shape-controlled synthesis of these Pd nanoparticles, much of the focus has been on the overall macroscopic description of the synthesis process and neither the local (surface) atomic geometry nor the explicit electronic structure were given enough attention, which is crucial for chemical catalysis. Notwithstanding, these microscopic details can be studied and probed via first-principles electronic structure calculations. Thus, in this present work, we examine the underlying atomic structure and energetics that influence the morphological evolution of Pd nanoparticles under an inorganic Br capping agent environment from first principles.

II. METHODOLOGY

A. Computational details

In this work, all density-functional theory (DFT) calculations are performed using the all-electron DMol^3 code[26,27] and the generalized gradient approximation (GGA) to the exchange-correlation functional is due to Perdew *et al.* (PBEsol)[28] which has been shown to perform well for both bulk and surface properties of transition metals.[29] The Kohn-Sham DFT orbitals are expanded in terms of a double-numerical localized basis set with polarization functions (DNP) where an element-dependent localization cutoff radius is used (i.e. 8.55 Bohr for Br and 9.98 Bohr for Pd, respectively). Scalar-relativistic corrections have also been included in all calculations.[26,27]

For the surface and adsorption models, we use a symmetric supercell slab approach with 25 Å of vacuum region. The low Miller-index Pd(100), (110), and (111) slabs are composed of 7 atomic layers (AL) with slab depths of 11.7 Å, 8.3 Å, and 13.5 Å, respectively. As for the high Miller-index surfaces, Pd(210) is modelled using 6 atomic layers parallel to the (110) terrace with a slab thickness of 15.7 Å (or an equivalent of 19 AL). Pd(211), Pd(311), and

Pd(331) all are modelled using 6 atomic layers parallel to the (111) surface and are thus 13.5 Å (18 AL), 15.3 Å (14 AL), and 12.5 Å (18 AL) thick, respectively. When relaxing the atomic geometries of the low Miller-index Pd surfaces, the inner-most 3 atomic layers of the slab are fixed to their bulk positions while relaxing the other outer-most atomic layers. Likewise for the high Miller-index surfaces, the inner-most 7 atomic layers of Pd(210) and Pd(331) and 6 inner-most atomic layers for Pd(211) and Pd(311) are fixed to their bulk positions. In a similar fashion, the outer-most atomic layers of these high Miller-index surfaces are fully relaxed. To account for the various surface coverages of Br on these Pd surfaces, larger surface supercells of Pd have been employed. We have carefully tested the convergence of required thickness of the low Miller-index surface slab models and extended that to the high Miller-index surface slab models.

The Brillouin-zone integrations are performed using Monkhorst-Pack **k**-point grids of $(12 \times 12 \times 12)$ for bulk Pd, $(12 \times 12 \times 1)$ for the $p(1 \times 1)$ surface unit cells of Pd(001) and Pd(111), and $(12 \times 8 \times 1)$ for that of Pd(110). For the $p(1 \times 1)$ surface unit cells of high Miller-index Pd surfaces, we use a **k**-point grid of $(7 \times 7 \times 1)$ for Pd(210) and Pd(311), $(12 \times 5 \times 1)$ for Pd(211), and $(5 \times 5 \times 1)$ for Pd(331). These **k**-point grids are then folded accordingly for the larger surface supercells used. We have also optimized both the atomic positions and lattice parameters of bulk palladium dibromide (PdBr$_2$) with a **k**-point grid of $(8 \times 12 \times 1)$. A thermal broadening of 0.1 eV has been used to improve the **k**-point convergence. With this setup, the total energies, forces on atoms and their displacements are converged to within 10^{-6} Ha (2.7×10^{-5} eV), 10^{-4} Ha/Bohr (5.1×10^{-3} eV/Å), and 10^{-4} Bohr (5.3×10^{-5} Å), respectively.

B. *Ab initio* (electrochemical) thermodynamics

To study the thermodynamic stability of these Br/Pd surface systems in its immediate Br chemical environment, we employ the well-established *ab initio* atomistic thermodynamics (*ai*AT), starting from DFT total energies. This has been discussed in great details in previous reports,[30–33] thus we will briefly outline this for our system. Firstly, we start by defining the clean surface energy of Pd, γ_{clean}, with

$$\gamma_{\text{clean}} = \frac{1}{2A}(E_{\text{Pd}}^{\text{slab}} - N_{\text{Pd}}^{\text{slab}} E_{\text{Pd}}^{\text{bulk}}) \quad , \qquad (1)$$

where A is the surface unit area, $E_{\mathrm{Pd}}^{\mathrm{slab}}$ the total energy of the clean Pd slab, $N_{\mathrm{Pd}}^{\mathrm{slab}}$ the corresponding number of Pd atoms in the slab, and $E_{\mathrm{Pd}}^{\mathrm{bulk}}$ the total energy of the bulk Pd.

Next, we will calculate the average binding energy of the Br adsorbate on Pd, $E_{\mathrm{b}}^{\mathrm{Br}}$ as well as the change in surface Gibbs free energy of adsorption, ΔG^{ad} as function of the change in the chemical potential of bromine, $\Delta\mu_{\mathrm{Br}}$ by following these equations:

$$E_{\mathrm{b}}^{\mathrm{Br}} = \frac{1}{N_{\mathrm{Br}}}(E_{\mathrm{Br/Pd}} - N_{\mathrm{Pd}}E_{\mathrm{Pd}}^{\mathrm{slab}} - \frac{N_{\mathrm{Br}}}{2}E_{\mathrm{Br}_2}) \quad , \tag{2}$$

$$\Delta G^{\mathrm{ad}}(\Delta\mu_{\mathrm{Br}}) \simeq \frac{1}{2A}(N_{\mathrm{Br}}E_{\mathrm{b}}^{\mathrm{Br}} - \Delta N_{\mathrm{Pd}}\mu_{\mathrm{Pd}} - N_{\mathrm{Br}}\Delta\mu_{\mathrm{Br}}) \quad , \tag{3}$$

where $E_{\mathrm{Br/Pd}}$ is the total energy of Br/Pd system. Here, $\Delta\mu_{\mathrm{Br}}$ is the change in the chemical potential of Br with respect to the Br$_2$ molecule (in the gaseous state), and likewise, E_{Br_2} and N_{Br} are the total energies of the Br$_2$ molecule and the number of Br atoms in the system, accordingly. In passing, the term $\Delta N_{\mathrm{Pd}}\mu_{\mathrm{Pd}}$ in Eq. 3 is only required when the total number of Pd atoms on the specific surface is different from that of the pristine clean surface. We note that vibrational and configurational effects of these systems have been neglected in this work, whereby the Gibbs free energy has been approximated by the calculated DFT total energy. This approximation has been successfully applied to predict the relative stability of surface structures in other adsorbate-substrate systems[31,34,35] where such effects are deemed to be small and thus will not change the overall conclusion in this work.

Given that these transition metal nanocatalysts often operate under an electrochemical environment (especially in fuel cell applications) as well, it is also interesting to study their nanomorphology evolution under the influence of an electrode potential, U. Here, we take after the procedure of Gossenberger et $al.$[36] where, within the aiAT approach, the atomic chemical potential, μ is reformulated with an electrochemical potential, $\tilde{\mu} = \mu + neU$ to mimic and describe the potential change of the adsorbate in solution with respect to the standard hydrogen potential, ΔU_{SHE} in standard state ($T = 298\,\mathrm{K}$ and $p = 1\,\mathrm{bar}$). Here, e and n are taken as the elementary charge and the charge of the species, respectively. Through this approach, ΔG^{ad} can be expressed using $\Delta U_{\mathrm{SHE}} = U - U_{\mathrm{SHE}}$ instead of the atomic chemical potential, $\Delta\mu_{\mathrm{Br}}$, by the following equation

$$\Delta G^{\mathrm{ad}}(\Delta U_{\mathrm{SHE}}) = \frac{N_{\mathrm{Br}}}{2A}\left(E_{\mathrm{b}}^{\mathrm{Br}} - \frac{1}{2}E_{\mathrm{Br}_2} - e(\Delta U_{\mathrm{SHE}} - U^0)\right) \quad , \tag{4}$$

where U^0 is the reduction potential of Br for the redox pair Br_2/Br^- (1.087 V).[37]

C. DFT-based equilibrium nanocrystal shape prediction

We now describe our approach to model the crystal shapes of the Pd nanoparticles in a Br chemical environment. From Eq. 1, we include the effect of Br on the clean surface free energy of Pd, γ_{clean} by adding the ΔG^{ad} term from Eq. 3 (or Eq. 4 for an electrochemical environment) in the following manner:

$$\gamma_{Br/Pd} \left(\Delta\mu_{Br}, \Delta U_{SHE}\right) = \gamma_{clean} + \Delta G^{ad} \left(\Delta\mu_{Br}, \Delta U_{SHE}\right) \quad , \tag{5}$$

where $\gamma_{Br/Pd}$ is now the surface free energy of the Br/Pd surface system which depends on either the atomic chemical potential $\Delta\mu_{Br}$ or the electrochemical potential ΔU_{SHE}. Having obtained the Br/Pd surface free energies from our DFT calculations from Eq. 5, we can now use these energies as *ab initio* input parameters into the Gibbs-Wulff shape model[38] to study the evolutionary equilibrium crystal shape (ECS) as a function of its adsorbate environment[31,33,39] – in both a Br chemical and electrochemical environment. Briefly, the mathematical equation of Gibbs-Wulff theorem is given by:

$$r(d) = \min_{hkl}[\alpha \cdot \gamma(\mu_i)] \quad , \tag{6}$$

where $r(d)$ represents the radius of crystal in vector direction, d and α is the constant. $\gamma(\mu_i)$ is the surface energy value as function of chemical potential of the component i. This then results in the Gibbs-Wulff polygon – a shape-focused theorem (and not on the size explicitly). Without the need to explicitly model the "real" nanoparticle (neither its size nor the number of atoms), one can provide an estimation of the nanoparticle ECS as a function of its immediate chemical environment.

It is well known that the size of the nanoparticle plays a huge role in its unique physical and chemical properties. Nonetheless, this is not the main point of this work (albeit also very important). Here, we want to stress how special additives (e.g. Br) could help in controlling the shape of the nanoparticles (rather than considering size-effects) and have explicitly addressed this morphological evolution via first-principles based ECS predictions. The ECS of the brominated Pd nanoparticle is predicted by considering the adsorption of

Br on all seven low and high Miller-index surfaces of Pd, namely the (100), (110), (111), (210), (211), (311), and (331) surfaces of Pd, at various surface coverages of Br.

III.   RESULTS AND DISCUSSION

A.   Bulk Pd, molecule Br_2 and clean Pd surfaces

Before studying the adsorption behaviour of Br on Pd, we first investigate the bulk properties of Pd, as well as some molecular properties of Br_2. The PBEsol-DFT calculated lattice constant (neglecting zero-point corrections) of bulk fcc Pd is $3.90\,\text{Å}$ and this agrees well with reported experimental values of $3.88\,\text{Å}$.[40] Our calculated bulk modulus and cohesive energy of Pd are $193\,\text{GPa}$ and $-4.28\,\text{eV}$, respectively, which are also in fair agreement with the experimental values ($181\,\text{GPa}$ and $-3.91\,\text{eV}$),[40,41] and are in-line with other reported theoretical results ($204\,\text{GPa}$ and $-4.43\,\text{eV}$).[40,42] The calculated Br–Br bond length and binding energy of Br_2 are $2.32\,\text{Å}$ and $-1.32\,\text{eV}$, respectively, and agree closely with reported experimental values of $2.28\,\text{Å}$ and $-1.22\,\text{eV}$.[41,43]

For the clean surfaces of Pd, we specifically consider the low Miller-index surfaces, namely

TABLE I. Calculated surface free energies (in eV/Å^2), c.f. Eq. 1, of various low and high Miller-index surfaces of pristine Pd. The specific nomenclature for the high Miller-index surfaces are also reported.[44]

Pd Surface	Nomenclature	DFT xc-functional	γ_{clean}
(100)	−	PBEsol[a]	0.115
		PBE[b]	0.093
(110)	−	PBEsol[a]	0.122
		PBE[b]	0.097
(111)	−	PBEsol[a]	0.099
		PBE[c]	0.082
		Exp.[c]	0.125
(210)	2(110)×(100)	PBEsol[a]	0.125
(211)	3(111)×(100)	PBEsol[a]	0.115
(311)	2(100)×(111)	PBEsol[a]	0.118
(331)	3(111)×(111)	PBEsol[a]	0.126

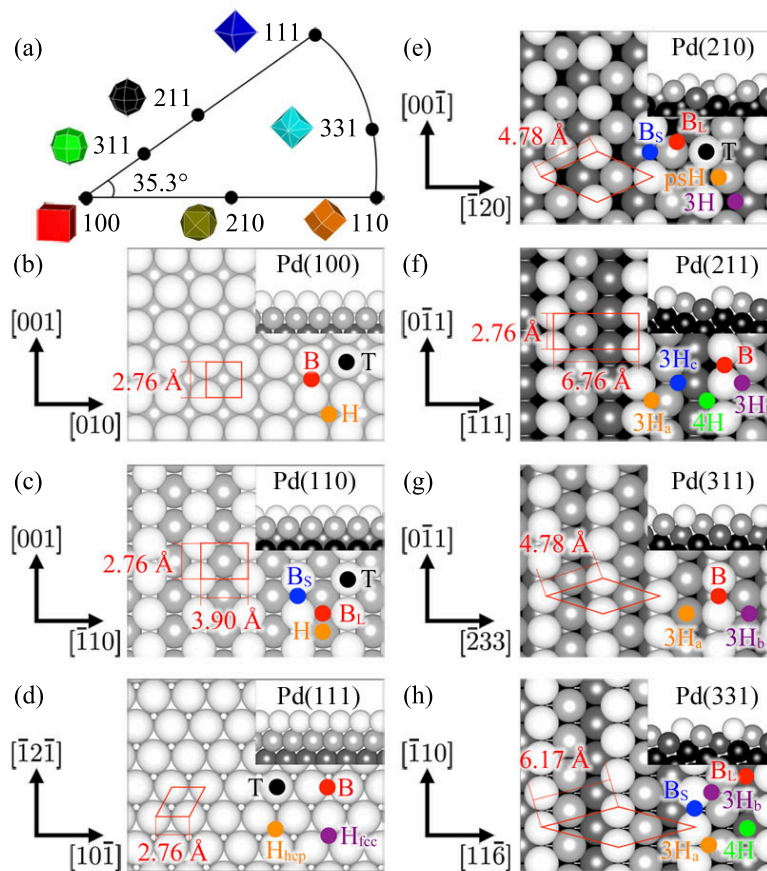[a] This work
[b] Reference 45
[c] Reference 46

FIG. 1. (Color online) (a) Stereographic projection of the various high Miller-index surfaces in relation to the low Miller-index surfaces for the fcc lattice. The top- and side-views of primitive surface unit cells (and the unique adsorbate binding sites) of the (b) (100), (c) (110), (d) (111), (e) (210), (f) (211), (g) (311), and (h) (331) of Pd are shown. The red lines indicate the primitive surface unit cells with length of edges displayed. With regards to the adsorbate binding sites on the low Miller-index surfaces, T represents the top site, B the bridge site, B_S the short bridge site, B_L the long bridge site, H the four-fold hollow site, H_{hcp} the hcp three-fold hollow site, H_{fcc} the fcc three-fold hollow site, and psH the pseudo hollow site. In addition to these sites, for the high Miller-index surfaces, 3H would then represent the three-fold hollow site, 4H the four-fold hollow site, and the subscript letters of H (namely, a, b, and c) represents the first, second, and third kind of sites, respectively.

the (100), (110), and (111) surface of Pd, as well as the following high Miller-index surfaces: (210), (211), (311), and (331) of Pd. These faceted surfaces are known to comprise of a certain combination of low Miller-index terraces and steps, and their explicit relationship is shown in Fig. 1a. The primitive surface unit cells of the these Pd surfaces are also indicated in Figs. 1b to 1h. Upon relaxing the atomic geometries of these surfaces, we report their DFT surface energies (c.f. Eq. 1) in Tab. I. Here we see that the surface energies of the low Miller-index Pd surfaces are lower (i.e. more stable) than that of the high Miller-index
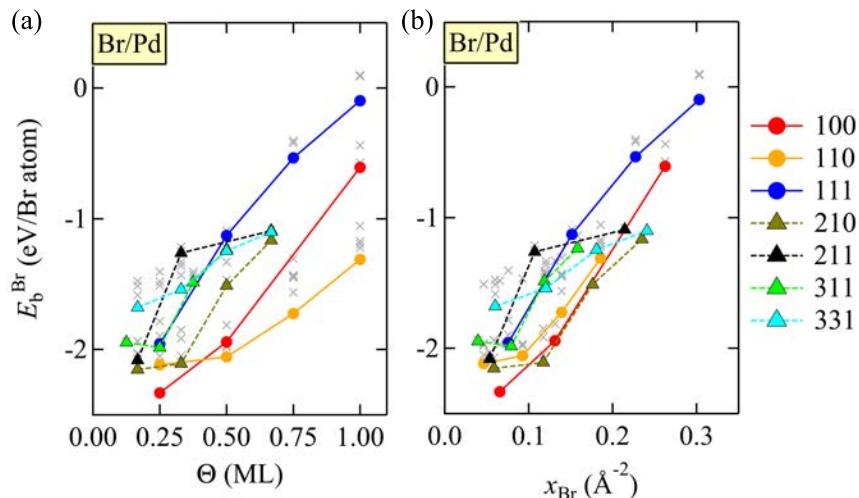
FIG. 2. (Color online) (a) Average binding energies of Br on Pd surfaces as a function of Br surface coverage, Θ, with respect to half the dissociation energy of Br_2 (i.e. $\frac{1}{2}E_{Br_2}$). (b) The same information in (a) but normalized with respect to the number of Br atoms per area, x_{Br}. Solid lines with filled circle dots trace the adsorption trend of the low Miller-index surfaces: 100 (red), 110 (yellow), and 111 (blue), while the dashed lines with filled triangle dots illustrate that of the high Miller-index surfaces: 210 (khaki green), 211 (black), 311 (light green), and 331 (cyan). Energetically less-favourable Br/Pd structures are shown as pale gray crosses.

surfaces, and these observations are in-line with previously reported values for Pd[32], as well as that found for other fcc transition metals (e.g. Cu).[47] This is easily rationalized by considering the number of metal bonds cut when generating these surfaces, and it will cost more energy (i.e. cutting more surface bonds) to cleave bulk metal to form these high Miller-index surfaces than the low Miller-index ones.[48,49]

B. Thermodynamical stability of Br/Pd surface structures

To date, no systematic studies of Br adsorption on Pd surfaces have been reported, either experimentally nor theoretically. Nevertheless, to build up such a study of Br adsorption on the Pd surfaces mentioned above, we have calculated the the average binding energies of Br on Pd surfaces as a function of their surface coverages, ranging from as low as 0.17 up to 1.00 monolayer (ML) surface coverage, for each unique binding site as illustrated in Figs. 1b to 1h using Eq. 2. To consider the energetic stability of Br on these binding sites as a function of its surface coverage, we have calculated close to 100 different Br/Pd surface structures. Given that it becomes to tedious and cumbersome to report all surface structures, we only

highlight the average binding energy of most stable Br/Pd surface structure for each surface as a function of surface coverage in Fig. 2a. Considering the energetics of all these Br/Pd structures, we find that the calculated average binding energy of Br on all considered surfaces of Pd increases with the increasing surface coverage of Br. This trend in average binding energies is indicative of a repulsive lateral interaction between surface Br atoms which will be analyzed and described further below in the text.

At low surface coverages of Br, we see that the average binding energies of the most stable chemisorbed Br on the various Pd surfaces converge to a value near $-2\,\mathrm{eV}$, with a small scattered distribution of $\pm\,0.5\,\mathrm{eV}$. At $0.25\,\mathrm{ML}$ surface coverage, we find that Br binds the strongest at the hollow site (H) on Pd(100) with an average binding energy of $-2.33\,\mathrm{eV}$. It is also interesting to find that Br binds strongly at the pseudo-hollow site (psH) on the less stable high Miller-index Pd (210) surface, and is almost as stable as Br on hollow sites for the low Miller-index surfaces of Pd(110) and Pd(111). This is unlike Br on other high Miller-index surfaces of Pd(311), Pd(331), and Pd(211), where the average binding energies become less favourable quickly as the surface coverage increases above $0.25\,\mathrm{ML}$.

For higher surface coverages of Br, the Br-Br interaction still remains repulsive and increases more rapidly with increasing surface coverages of Br, with Br binding most favourably on the more open Pd(110) – more so than on close-packed Pd(111). In particular, for the Br/Pd(110), at $0.5\,\mathrm{ML}$, Br occupies the hollow site with an average binding energy of $-2.06\,\mathrm{eV}$, and increasing the surface coverage to $0.75\,\mathrm{ML}$, Br then preferentially (but less strongly) binds to mixed hollow and short-bridge sites, with a binding energy of $-1.72\,\mathrm{eV}$. Finally, at the full $1\,\mathrm{ML}$, this binding energy value becomes even less favourable (i.e. $-1.22\,\mathrm{eV}$) when Br adsorbs on the long-bridge sites.

In addition, to discuss the average binding energy trend as a function of the normalized surface area for all considered Pd surfaces, we have also plotted this information in Fig. 2b. Here we find that the tendency in the average binding energy trend (per atom per area) supports our discussion above, and indeed confirms the lateral Br–Br repulsive behaviour with increasing surface coverage of Br.

Having obtained these DFT-calculated average binding energies of Br on Pd surfaces, we now couple these values to the aiAT model as described above. Specifically, the change in the Gibbs free energy of Br adsorption for each Pd surface, ΔG^{ad} (c.f. Eq. 3) is calculated and expressed as a function of the Br chemical potential change, $\Delta\mu_{\mathrm{Br}}$, as shown in Fig. 3.
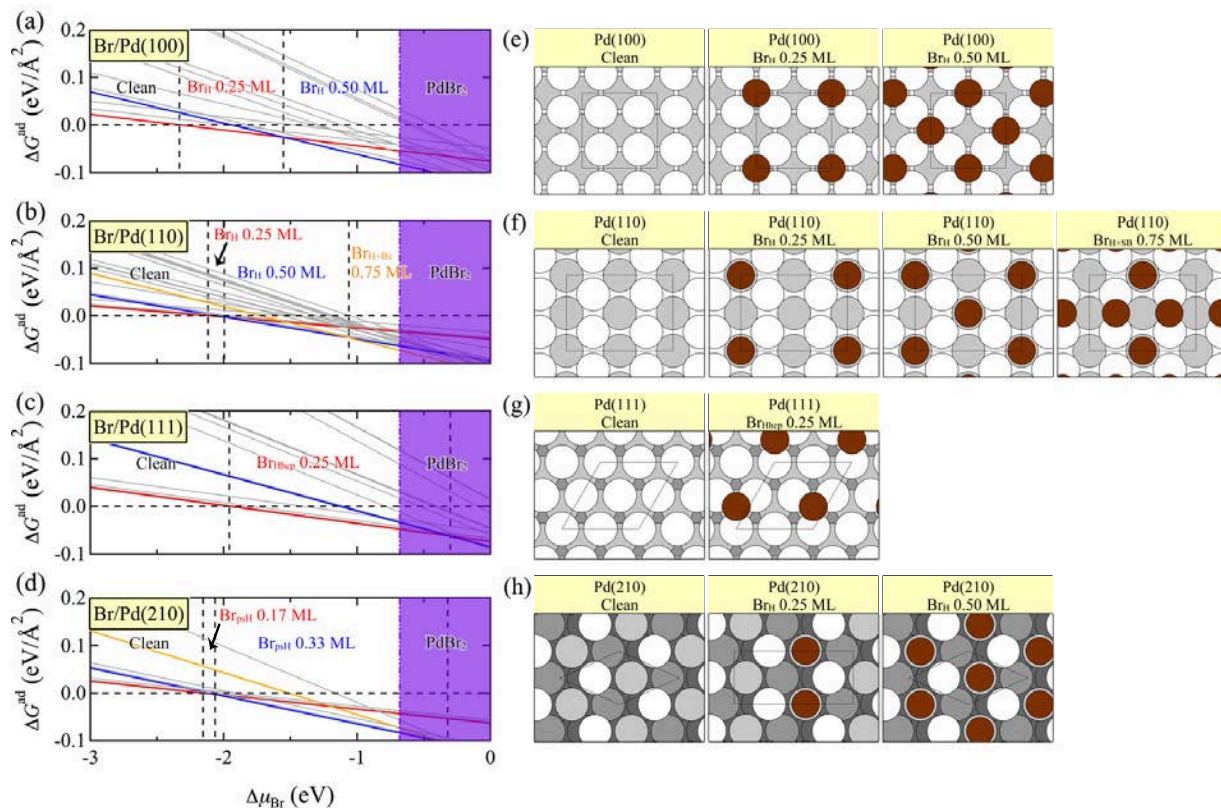
FIG. 3. (Color online) Calculated Gibbs free energy of adsorption of Br, ΔG^{ad} on (a) Pd(100), (b) Pd(110), (c) Pd(111), and (d) Pd(210) as a function of the Br chemical potential change, $\Delta\mu_{\mathrm{Br}}$. The horizontal dashed line (at $\Delta G^{\mathrm{ad}} = 0$) refers to the stable clean (Br-free) Pd surface. For each surface, the red, blue and yellow lines indicate the first, second, and third stable surface phase with increasing $\Delta\mu_{\mathrm{Br}}$, respectively. Other less stable surface structures are represented in gray lines. To guide the eye, the vertical black dashed lines indicate a surface phase change in stability, while the shaded purple region on the right hand side denotes the region of stability for bulk palladium dibromide, PdBr$_2$. The top-view of the stable surface structures are shown in (e) for Br/Pd(100), (f) Br/Pd(110), (g) Br/Pd(111), and (h) Br/Pd(210). The dark brown circles represent the bromine atoms while the white, light gray, and dark gray circles refer to the first, second, and third outermost Pd surface layers of the slab, respectively.

In particular, to account for the region of high Br chemical potentials, we consider the formation of bulk palladium dibromide, PdBr$_2$ and calculate its enthalpy of formation to be -0.68 eV/Br atom.

In Fig. 3a, at low $\Delta\mu_{\mathrm{Br}}$, the clean Pd(100) surface is the most stable, and with increasing exposure to Br, the $p(2 \times 2)$-Br$_{\mathrm{H}}$ (i.e. with Br adsorbed at the hollow site at $0.25\,\mathrm{ML}$) is formed when $\Delta\mu_{\mathrm{Br}} = -2.33\,\mathrm{eV}$, followed by the $0.5\,\mathrm{ML}$ $p(2 \times 2)$-2Br$_{\mathrm{H}}$ at $\Delta\mu_{\mathrm{Br}} = -1.55\,\mathrm{eV}$, and eventually bulk palladium dibromide (PdBr$_2$) at $-0.68\,\mathrm{eV}$. For Pd(110)(in Fig. 3b), upon Br adsorption, a rather small window of surface stability is seen for the $0.25\,\mathrm{ML}$ structure

$(p(2 \times 2)\text{-Br}_\text{H})$, followed consecutively by the 0.5 and 0.75 ML structures (i.e. $p(2 \times 2)\text{-2Br}_\text{H}$ and $p(2 \times 2)\text{-3Br}_\text{H}$, respectively), and finally bulk PdBr_2. As seen in Fig. 3c, Br on Pd(111) shows only one stable surface structure with Br in the hcp hollow site at 0.25 ML $(p(2 \times 2)$ - $\text{Br}_{\text{H}_\text{hcp}})$, before the onset of bulk PdBr_2. For comparison, we have also included the ΔG^ad plot for the high Miller-index Br/Pd(210) surface system in Fig. 3d.

We notice that the surface phase transitions start to occur much earlier for surface systems with an intrinsically less stable clean surface free energy and stronger average binding energy of Br (e.g. for Pd(100) and Pd(210)). Although instructive, these ΔG^ad provide phase stability information for individual brominated surface structures with reference to their respective clean surfaces. Thus, to relate and compare the relative stabilities of all the brominated surfaces of Pd in a more unified way, we now consider the adsorbate-modified surface free energy, $\gamma_\text{Br/Pd}$ of these Br/Pd surface systems via the Eq. 5, and plot the variation of $\gamma_\text{Br/Pd}$ as a function of $\Delta\mu_\text{Br}$ and the corresponding electrode potential, ΔU_SHE in Fig. 4. For low values of ΔU_SHE, the Br_2 gas phase is thermodynamically more stable than the Br^- ion, while for values of ΔU_SHE higher than 1.087 V, the Br^- ion dominates, pushing the equation $\frac{1}{2}\text{Br}_2 + e^- \leftrightarrows \text{Br}^-$ to the right.

C. Environment-dependent morphology of brominated Pd

Given that ΔG^ad is always negative in this case, the adsorbate-modified surface free energies are lowered (hence, more stable) as compared to γ_clean. Using these free energy curves, we then predict and trace the ECS morphological evolution of Br/Pd at the corresponding $\Delta\mu_\text{Br}$ and ΔU_SHE as shown in Fig. 5. To highlight and emphasize the importance of considering high Miller-index surfaces when modelling morphology evolution of nanoparticles, we have plotted the ECSs with only low Miller-index surfaces (in Figs. 5a and 5c), and those with both low and high Miller-index surfaces (in Figs. 5b and 5d) separately.

Free of Br, the absorbate-free Pd nanoparticle maximizes the exposure of the (111) facet, with the next less stable surfaces (mainly the Pd(100) surface) displayed due to geometric constraints. This is easily rationalized by considering the relative γ_clean (in both Tab. I and Fig. 4) where Pd(111) is the most stable clean surface. This results in the so-called (100)-truncated cuboctahedron shape, which is the most common and natural shape for most fcc metallic nanoparticles.[31]
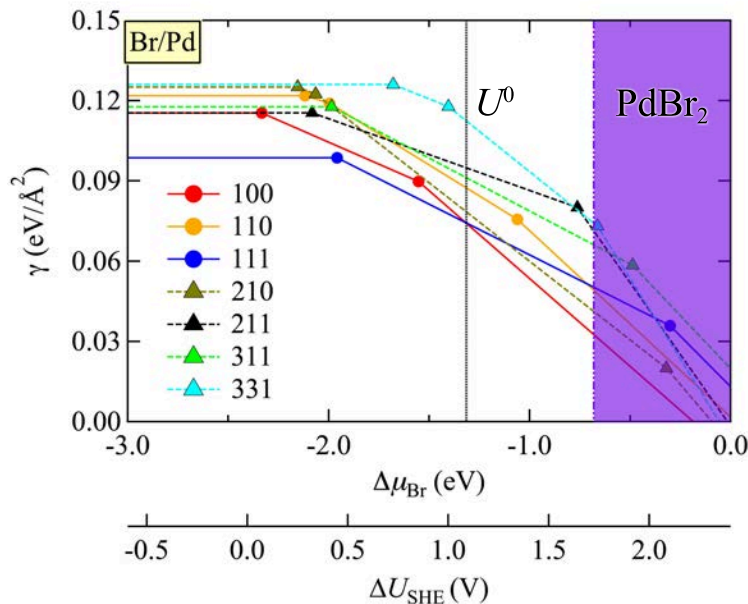
13

FIG. 4. (Color online) Calculated surface free energy of brominated Pd surfaces as a function of the Br chemical potential change, $\Delta\mu_{Br}$, and the corresponding electrode potential with respect to the standard hydrogen electrode, ΔU_{SHE}. The variation of surface free energy for the low Miller-index surfaces are traced using solid lines with filled circle dots while those for the high Miller-index surfaces are shown in dashed lines with filled triangle dots. To guide the eye, the black vertical dashed line indicates the reduction potential of Br ($U^0 = 1.09$ V), while the shaded purple region on the right hand side denotes the region of stability for bulk palladium dibromide, $PdBr_2$.

At very low exposures of Br (at $\Delta\mu_{Br} = -1.9$ eV and $\Delta U_{SHE} = 0.5$ V), this (100)-truncated cuboctahedron is modified slightly by the enlargement of the Br/Pd(100) facet and the small appearance of the Br/Pd(210) surface at the edges. Again, this corroborates with our free surface energy curves in Fig. 4 where the (100) surface of Pd is stabilized via the adsorption of 0.25 ML of Br at the hollow sites.

At higher $\Delta\mu_{Br} = -1.3$ eV (and $\Delta U_{SHE} = 1.1$ V), almost equal amounts of the (100), (111) and (210) of Br/Pd is formed, as a result of Br shaping and causing the nanoparticle to become more spherical in shape. This is the result of the large stabilization of both the (100) and (210) surfaces of Pd upon adsorbing Br at 0.25 and 0.33 ML local surface coverage, respectively as seen in Fig. 4. We strongly stress and contrast the consequence of not considering higher Miller-index surfaces by referring to the different ECSs in Figs. 5c and 5d where this *rounding* of the nanoparticle would otherwise be overlooked.

Now, at $\Delta\mu_{Br} = -0.7$ eV (and $\Delta U_{SHE} = 1.7$ V), the nanoparticle ECS completely and drastically transforms into the cubic-like shape with the (100) surface of Pd encapsulating
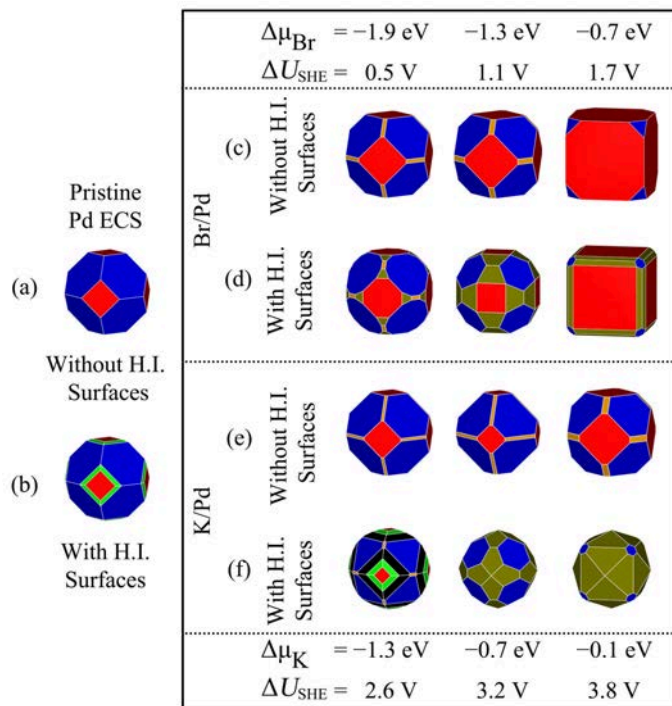
FIG. 5. (Color online) Predicted morphology evolution of the Pd nanoparticle under Br (and K) (electro)chemical environment as functions of $\Delta\mu_{\text{Br}}$ (and $\Delta\mu_{\text{K}}$) and ΔU_{SHE}. The pristine morphology is described with considering (a) only low Miller-index surfaces, and (b) both low and high Miller-index (H.I.) facets, respectively. Changes to the equilibrium crystal shapes are also shown for the two cases: For Br/Pd with the consideration of (c) only low Miller-index surfaces, and (d) both low and high Miller-index surfaces, and likewise in (e) and (f) for K/Pd, accordingly.

the whole nanoparticle, with Br/Pd(210) lining the edges and very small (111) facets of Pd at the corners of the cube. Once again, the Br/Pd(210) surface structures at the edges would have been omitted if high Miller-index surfaces were excluded in the morphology modeling (c.f. Figs. 5c and 5d). This drastic transformation to the nanocube shape is greatly facilitated by the strong Br binding energy modification to the surface free energy of Pd(100), lowering it much more than that of the other surfaces of Pd. This is achieved by adsorbing 0.5 ML of Br at the hollow site of Pd(100). We note in passing that if one were to only consider the average binding energy of Br on Pd as a function of surface coverage (c.f. Fig. 2) and not include such atomic thermodynamic analysis, one might be easily misled to think that the 0.25 ML structure ($p(2 \times 2)$-Br_{H}) for Pd(100) should be the most stable (and thus most relevant) structure to proceed for further investigation. It is thus important to draw attention here that the relevant surfaces/facets to analyze should be the ones exposed on the nanoparticle (in its appropriate chemical environment).

As reported in Ref. 21, KBr solution was introduced in the synthesis of Pd nanocubes, demonstrating that Br anions served as the key inorganic capping agent for the (100) surface of Pd. Here, we have also investigated the possible role of the K cation which is often ignored. To understand the stability of various K/Pd surface systems, we adsorb K in the various symmetry-unique sites on the (100), (110), (111), (210), (211), (311), and (331) surfaces of Pd, at various surface coverages of K, as outlined above (c.f. Fig. 1). We find that the average binding energies of K on Pd are less favorable than those of Br (see Supporting Information, Fig. 1), confirming its role as a spectator ion while Br preferentially binds on Pd surfaces. Likewise, we use the concept of aiAT with these DFT-derived energetics as inputs and plot the free energy lines (in Supporting Information, Figs. 3 and 4). For the K/Pd system, the (111) surface of Pd is found to be the most stable surface for all exposures of K, and the resultant ECSs are shown in Figs. 5e (without high Miller-index surfaces of Pd considered) and 5f (with the inclusion of high Miller-index Pd surfaces). Interestingly, as seen in Fig. 5e, the truncated cuboctahedron nanoshape is preserved when only low Miller-index surfaces are considered, while the importance of the high Miller-index surfaces of Pd is once again demonstrated for higher exposures of K, with the K/Pd(210) facets enveloping the nanoparticle, forming a tetrakishexahedron. In this case, Pd nanocubes are not predicted, and again lends evidence to the spectator role of K ions in the shape-control synthesis of Pd nanocubes, as suggested by experiments.[21]

IV. CONCLUSIONS

In summary, we study the chemisorption of Br (and K) on the low and high Miller-index surfaces of Pd, such as (100), (110), (111), (210), (211), (311), and (331) through first-principles DFT calculations. We calculate the surface energies, as a function of the (electro)chemical potential change, accounting for the equilibrium crystal shape evolution of Pd nanoparticles in its immediate chemical environment. We clearly demonstrate the atomic origin of the role of Br in controlling the shape of Pd nanostructures, providing the detailed atomic structure of Br/Pd(100) exposed facet (i.e. $p(2 \times 2)$-2Br$_H$ at 0.5 ML surface coverage), and incontrovertibly showing the important role of high Miller-index surfaces in nanomorphological modeling. Here, we also allude the spectator role of the K cation. Given the clear importance and advantages of shape-sculptured nanoarchitectures in many

modern-day technologies, having a quantitative atomic picture of the surface chemistry and physics of these nanoparticles will be essential in a rational and systematic design of more selective and active nanocatalysts.

* Corresponding author. E-mail: aloysius.soon@yonsei.ac.kr

[1] A. R. Tao, S. Habas, and P. Yang, Small **4**, 310 (2008).

[2] S. E. F. Kleijn, S. C. S. Lai, M. T. M. Koper, and P. R. Unwin, Angew. Chem. Int. Ed. **53**, 3558 (2014).

[3] C. Wang, H. Daimon, T. Onodera, T. Koda, and S. Sun, Angew. Chem. Int. Ed. **47**, 3588 (2008).

[4] T. H. Yu, T. Hofmann, Y. Sha, B. V. Merinov, D. J. Myers, C. Heske, and W. A. G. III, J. Phys. Chem. C **117**, 26598 (2013).

[5] K. An and G. A. Somorjai, Chem. Cat. Chem. **4**, 1512 (2012).

[6] M. P. Pileni, J. Phys.: Condens. Matter **23**, 503102 (2011).

[7] K. Zhou and Y. Li, Angew. Chem., Int. Ed. **51**, 602 (2012).

[8] A. S. Barnard and L. A. Curtiss, Nano Lett. **5**, 1261 (2005).

[9] G. A. Somorjai, H. Frei, and J. Y. Park, J. Am. Chem. Soc. **131**, 16589 (2009).

[10] I. A. Suleiman, M. W. Radny, M. J. Gladys, P. V. Smith, J. C. Mackie, E. M. Kennedy, and B. Z. Dlugogorski, J. Phys. Chem. C **115**, 13412 (2011).

[11] T. Roman and A. Groß, Phys. Rev. Lett. **110**, 156804 (2013).

[12] S. E. Lohse, N. D. Burrows, L. Scarabelli, and L. M. Liz-Marzán, Chem. Mater. **26**, 34 (2014).

[13] Y. Sakabe, Curr. Opin. Solid St. M. **2**, 584 (1997).

[14] H. Kishi, Y. Mizuno, and H. Chazonoj, Jpn. J. Appl. Phys. **42**, 1 (2003).

[15] S. Kishore, J. A. Nelson, J. H. Adair, and P. C. Eklund, J. Alloy. Compd. **389**, 234 (2005).

[16] M. Yamauchi, R. Ikeda, H. Kitagawa, and M. Takata, J. Phys. Chem. C **112**, 3294 (2008).

[17] H.-U. Blaser, A. Indolese, A. Schnyder, H. Steiner, and M. Studer, J. Mol. Catal. A: Chem. **173**, 3 (2001).

[18] Y. Li, X. M. Hong, D. M. Collard, and M. A. El-Sayed, Org. Lett. **2**, 2385 (2000).

[19] P. Cotugno, M. Casiello, A. Nacci, P. Mastrorilli, M. M. Dell'Anna, and A. Monopoli, J. Organomet. Chem. **752**, 1 (2014).

[20] A. Trinchero, A. Hellman, and H. Grönbeck, Surf. Sci. **616**, 206 (2013).

[21] H.-C. Peng, S. Xie, J. Park, X. Xia, and Y. Xia, J. Am. Chem. Soc. **135**, 3780 (2013).

[22] X. Xia, S. Xie, M. Liu, H.-C. Peng, N. Lu, J. Wang, M. J. Kim, and Y. Xia, Proc. Natl. Acad. Sci. **110**, 6669 (2013).

[23] Y. Xiong, H. Cai, B. J. Wiley, J. Wang, M. J. Kim, and Y. Xia, J. Am. Chem. Soc. **129**, 3665 (2007).

[24] W. Niu, L. Zhang, and G. Xu, ACS Nano **4**, 1987 (2010).

[25] A.-X. Yin, X.-Q. Min, Y.-W. Zhang, and C.-H. Yan, J. Am. Chem. Soc. **133**, 3816 (2011).

[26] B. Delley, J. Chem. Phys. **92**, 508 (1990).

[27] B. Delley, J. Chem. Phys. **113**, 7756 (2000).

[28] J. P. Perdew, A. Ruzsinszky, G. I. Csonka, O. A. Vydrov, G. E. Scuseria, L. A. Constantin, X. Zhou, and K. Burke, Phys. Rev. Lett. **100**, 136406 (2008).

[29] L. Schimka, J. Harl, A. Stroppa, A. Grüneis, M. Marsman, F. Mittendorfer, and G. Kresse, Nat. Mater. **9**, 741 (2010).

[30] K. Reuter, C. Stampfl, and M. Scheffler, *Ab initio* Atomistic Thermodynamics and Statistical Mechanics of Surface Properties and Functions, in *Handbook of Materials Modeling*, Vol. 1 (Springer Berlin Heidelberg, 2005).

[31] X. Duan, O. Warschkow, A. Soon, B. Delley, and C. Stampfl, Phys. Rev. B **81**, 075430 (2010).

[32] F. Mittendorfer, N. Seriani, O. Dubay, and G. Kresse, Phys. Rev. B **76**, 233413 (2007).

[33] T. Lee, B. Delley, C. Stampfl, and A. Soon, Nanoscale **4**, 5183 (2012).

[34] C. Stampfl, Catal. Today **105**, 17 (2005).

[35] J. Rogal, K. Reuter, and M. Scheffler, Phys. Rev. B **75**, 205433 (2007).

[36] F. Gossenberger, T. Roman, and A. Groß, Surf. Sci. DOI: 10.1016/j.susc.2014.01.021.

[37] G. Inzelt, *Encyclopedia of Electrochemistry, Inorganic Chemistry CH.1. Standard Potentials*, edited by A. J. Bard, M. Stratmann, F. Scholz, and C. J. Pickett, Vol. 7A (Wiley-VCH, Weinheim, 2006).

[38] G. Wulff, Z. Kristallogr. **34**, 449 (1901).

[39] A. Soon, M. Todorova, B. Delley, and C. Stampfl, Phys. Rev. B **75**, 125420 (2007).

[40] L. Schimka, J. Harl, and G. Kresse, J. Chem. Phys. **134**, 024116 (2011).

[41] C. Kittel, *Introduction to Solid State Physics,* 8th ed. (John Wiley & Sons, 2005).

[42] A. D. Corso, J. Phys.: Condens. Matter **25**, 145401 (2013).

[43] A. Erbil, G. Dresselhaus, and M. S. Dresselhaus, Phys. Rev. B **25**, 5451 (1982).

[44] A. Groß, *Theoretical Surface Science: A Microscopic Perspective*, 2nd ed. (Springer-Verlag Berlin Heidelberg, 2009) pp. 16–17.

[45] N. E. Singh-Miller and N. Marzari, Phys. Rev. B **80**, 235407 (2009).

[46] J. L. F. Da Silva, C. Stampfl, and M. Scheffler, Surf. Sci. **600**, 703 (2006).

[47] J. L. F. Da Silva, C. Barreteau, K. Schroeder, and S. Blügel, Phys. Rev. B **73**, 125402 (2006).

[48] I. Galanakis, G. Bihlmayer, V. Bellini, N. Papanikolaou, R. Zeller, S. Blügel, and P. H. Dederichs, Europhys. Lett. **58**, 751 (2002).

[49] I. Galanakis, N. Papanikolaou, and P. H. Dederichs, Surf. Sci. **511**, 1 (2002).